Tunable and broadband S-band loop-gap-resonator for nitrogen vacancy centers in diamond

by

Erik Roger Eisenach

B.S., The Citadel, The Military College of South Carolina (2015)

Submitted to the Department of Electrical Engineering and Computer Science
in partial fulfillment of the requirements for the degree of

Master of Science in Electrical Engineering and Computer Science

at the

MASSACHUSETTS INSTITUTE OF TECHNOLOGY

June 2018

Author . . . .
Department of Electrical Engineering and Computer Science
May 23, 2018

Certified by. . . . .
Dirk Englund
Associate Professor, Massachusetts Institute of Technology
Thesis Supervisor

Certified by. . . . .
Danielle Braje
Assistant Group Leader, Lincoln Laboratory
Thesis Supervisor

Accepted by . . . .
Leslie A. Kolodziejski
Chairman, Department Committee on Graduate Theses

Tunable and broadband S-band loop-gap-resonator for nitrogen vacancy centers in diamond

by

Erik Roger Eisenach

Submitted to the Department of Electrical Engineering and Computer Science
on May 23, 2018, in partial fulfillment of the
requirements for the degree of
Master of Science in Electrical Engineering and Computer Science

Abstract

In this thesis, the loop gap resonator (LGR) is presented as a mechanism for the delivery of resonantly enhanced and uniform microwave fields to large volume samples of nitrogen vacancy (NV) centers in diamond. Specifically, an S-band tunable LGR and its constituent excitation circuitry are designed that allow directionally uniform, strong, homogeneous, and broadband microwave (MW) driving of an NV ensemble over an area larger than 32 mm^2. Two methods of coupling to the resonator are implemented and discussed. The LGR design, based on the anode block of a cavity magnetron, demonstrates an average field amplitude of 5 gauss at 43 dBm of input power, and achieves a peak-to-peak field uniformity of 89.5% over an area of 32.2 mm^2 and 97% over an area of 11 mm^2. The broad bandwidth of the LGR is capable of addressing all resonances of an NV ensemble for bias magnetic Fields up to 20 gauss. Furthermore, with cavity ring-down-times in the tens of nanoseconds, the resonator is compatible with the pulsed MW techniques necessary for a wide range of NV-diamond applications.

Thesis Supervisor: Dirk Englund
Title: Associate Professor, Massachusetts Institute of Technology

Thesis Supervisor: Danielle Braje
Title: Assistant Group Leader, Lincoln Laboratory

Acknowledgments

This is the acknowledgements section. You should replace this with your own acknowledgements.

Contents

List of Figures

List of Tables

Chapter 1

The Nitrogen Vacancy Center in Diamond

1.1 Introduction

The nitrogen-vacancy (NV) defect center in diamond is currently of great interest for many applications in quantum sensing [39, 3, 14, 29, 12, 19] and quantum information [7, 18, 16] due to its many outstanding properties, which include long room temperature coherence times [3] and simplicity of optical quantum state initialization and readout [36, 22]. An active area of effort is NV magnetometry, with recent demonstrations of measurement modalities ranging from scanning magnetic microscopy [12] to wide-field imaging [31] to bulk magnetometry [41]. Many of these modalities address ensembles of NV centers and therefore require strong and uniform microwave (MW) field driving, often over mm length scales. In this thesis I discuss the design considerations of a suitable MW delivery mechanism, fabricate a hole-and-slot type loop gap resonator (LGR), and evaluate its performance for NV applications.

As an introduction to the field of quantum sensing using NV centers Chapter 1 deems to introduce the photophysics of the NV[1], the NVs use in continuous wave and pulsed magnetometry schemes, the importance of uniform microwave (MW) driving

---

[1]A detailed derivation of the NV level structure using group theoretic approach can be found in []

and previous resonant enhancement techniques, along with an introduction to the hole-and-slot type loop gap resonator featured in Chapters 2-5 and a discussion of popular coupling techniques.

Chapter 2 gives a detailed theoretical analysis of the loop gap resonator and its use in experiments utilizing electron spin resonance (ESR). It also steps through the design process of the LGR and excitation circuitry and discusses the considerations involved when choosing the device geometry and attempting to match the LGR over a wide bandwidth.

Chapter 4 discusses the MW field distribution and strength provided by the fundamental mode of the manufactured LGR using both experiment and simulations.

Chapter 5 provides an analysis of the device's uses in NV magnetometry as well as an outlook to future of the LGR for quantum sensing.

1.2   The NV Physical and Electronic Structure

The negatively-charged NV color center (NV$^-$) is a deep band gap impurity within the diamond crystal lattice. Its inclusion in the C_{3v} point group permits a $^3A_2$ symmetric spin-triplet ground state and an excited ^3E state separated by a zero phonon line (ZPL) of 637nm [Fig 1-1 (a)] [26]. The ground state spin triplet is split via spin-spin interactions giving rise to a zero field splitting separating the $|m_s = 0\rangle$ from the $|m_s = \pm 1\rangle$ states by 2.87GHz (D_{gs}). The NV Hamiltonian, neglecting

Application of a static magnetic field B$_0$ splits the $|m_s = \pm 1\rangle$ levels via Zeeman interaction proportional to the projection of the field onto the NV symmetry axis. When the NV is driven into one of these states and optically excited (generally achieved using 532nm CW or pulsed laser) it undergoes phononic-relaxation and settles into the corresponding sublevel of the excited state. These sublevels allow the NV to preferentially decay back down to the $|0\rangle$ ground state via an inter-system crossing and metastable state which are separated in the infrared. This non-spin-conserving process therefore provides the mechanism of spin polarizing the NV for continued MW driving. The NV spin state can then be read out by sweeping the driving microwave
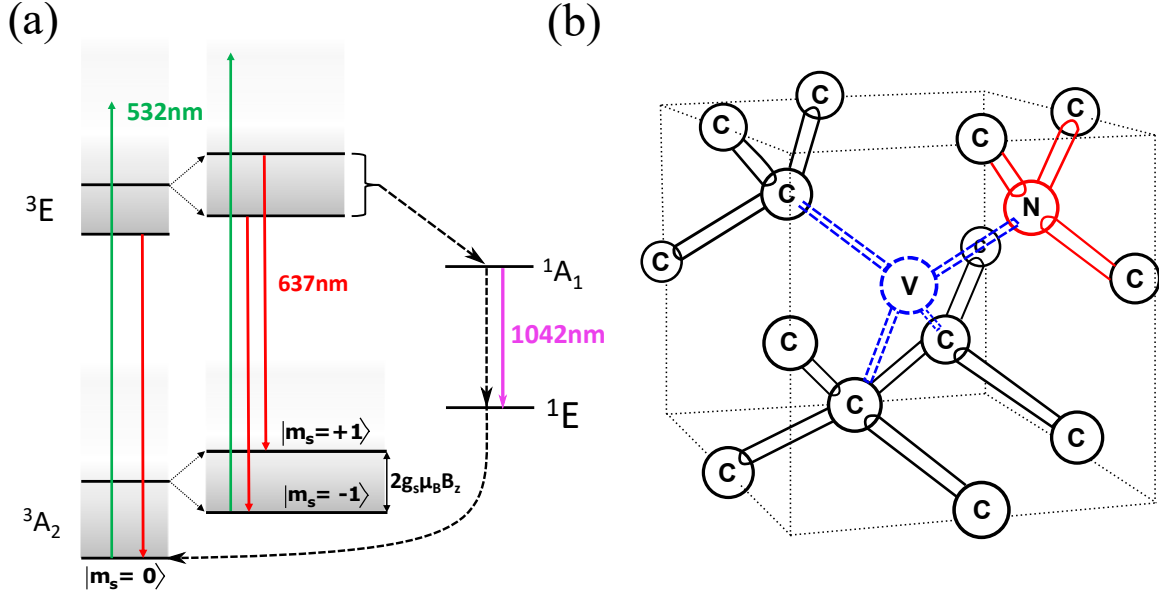
Figure 1-1: **The NV center a)** The NV level structure **b)** One of four crystal orientations of the NV.

field and monitoring NV fluorescence in the visible band. A drop in fluorescence at a particular driving frequency indicates electron spin resonance (ESR) which can be monitored via lock-in amplification for any detuning due to a change in the external field[22, 33]. Since the NV can exist in one of four possible orientations—each orientation being equally likely—the ESR can be separated into eight distinct non-degenerate resonances which probe different field components. The various orientations act as basis vectors which collectively span the space and allow the total vector field to be reconstructed [22].

1.3   Vector Magnetometry with NV Centers

As mentioned in section 1.2, the C_{3v} symmetry of diamond allows NV centers to be aligned in four different orientations in the lattice. Since, at fields lower than 10 mT, the Zeeman splitting of the $|\pm1\rangle$ is proportional to the vector field projection along the NV symmetry axis[2] (B_z) the energy shifts can be determined by $g_s \mu b \mathbf{B} \cdot \mathbf{u}_n$ where

---

[2]At these low fields the terms in the NV Hamiltonian (see equation **??**) that are proportional to the perpendicular component of the field are suppressed to order $\sim B_{xy}^2/D_{gs}$ and can therefore be neglected[39]

$\mathbf{u}_n$ ($n = 1, 2, 3, 4$) is the unit vector along the $\mathrm{n^{th}}$ NV axis. By either sequentially or simultaneously measuring the Zeeman splitting between either the $|0\rangle \leftrightarrow |+1\rangle$ or $|0\rangle \leftrightarrow |-1\rangle^3$ transitions of all four orientations, one can reconstruct the total vector field by generating the vector components (B_x, B_y, and B_z) from the projection along each of the crystallographic axes [24, 37].

1.3.1   NV Ensemble Magnetic Sensitivity

The magnetic sensitivity

1.3.2   Continuous Wave Magnetometry

For continuous wave magnetometry the ESR frequencies are continuously monitored (often using lock in amplification) since the external magnetic field is imprinted in their spectral positions ω_+ and ω_- [Fig ??]. As mentioned in section 1.3, the four orientations of the NV in the diamond crystal lattice therefore result in eight distinct resonances when split by an external biasing field (B_0). Monitoring a minimum of three out of four resonances allows for the full vector reconstruction of the field. An infinitesimal additional magnetic field variation δB shifts the resonances away from the known spectrum and the change in NV fluorescence, which is given by $\left(\frac{\partial \beta}{\partial B}\right) \cdot \delta B \cdot \tau$ [33], is measured in the laboratory. The shot-noise limited sensitivity is then given as,

$$\eta_{cw} \approx \frac{\hbar}{\mathrm{g_s \mu_B}} \frac{\Delta\omega\sqrt{\tau}}{C\sqrt{N\beta}}.$$

The signal contrast C can be increased by driving the NV with stronger MW fields at the expense of power-broadening the linewidth $\Delta\omega$. However, the linewidth can be decreased down to a limit given the inhomogeneous dephasing time T_2^* by reducing the laser and MW excitation strength [15], effectively decreasing the number of collected

---

[3]The transition $|-1\rangle \leftrightarrow |+1\rangle$ can also be employed which yields the benefit that the energy shift becomes $2\mathrm{g_s \mu_b}\mathbf{B}$ and therefore provides twice the signal over the other two transitions while simultaneously mitigating temperature effects [29]. However, this requires treatment of the full three-level spin system since the $|-1\rangle \leftrightarrow |+1\rangle$ splitting is a non-dipole allowed transition.

photons per measurement β. An optimization of contrast C, linewidth $\Delta\omega$, and collection β yields an optimized sensitivity of [30]

$$\eta_{cw} \approx \frac{2\hbar}{g_s\mu_B} \frac{1}{C\sqrt{N\beta T_2^*}}.$$

1.3.3 Pulsed Ramsey-type Magnetometry

Strong microwave driving in a CW experiment broadens the ESR linewidth causing a reduction in magnetometer sensitivity. To take advantage of strong driving fields without incurring the effects of MW or pump laser power broadening, DC fields can be measured using a Ramsey pulse sequence. In this scheme microwave driving, spin polarization and sensing are all separated in time [Fig 1-2(a)]. After spin polarizing the NV electron spin into the $m_s = 0$ ground state, a resonant microwave pulse of length $\pi/2$ creates a superposition of the $|0\rangle$ and $|+1\rangle$ energy levels,

$$|\Psi\rangle = \frac{1}{\sqrt{2}}(|0\rangle + e^{i\phi}|1\rangle),$$

where the accumulated phase after precession time τ is $\phi = 2\pi\gamma B\tau$ where B is the amplitude of the magnetic field to be determined and $\gamma = g_s\mu_B/h = 2.8$ MHz/gauss the NV electron spin gyromagnetic ratio. Following the precession interval, a second $\pi/2$ MW pulse projects the spin back onto the quantization axis which is measured in the laboratory as a population difference between $|0\rangle$ and $|+1\rangle$, and read out optically through the spin dependent fluorescence of the NV center. Sensitivity is therefore improved by increasing the free precession time τ in order to maximize the accumulated phase, however, dipolar coupling to other magnetic impurities in the spin bath randomizes the accumulated phase after time T_2^*, the inhomogeneous NV dephasing time. Sensitivity in this scheme is optimized when the NV is allowed to precess in the magnetic field for $\tau \sim T_2^*$ and is given by

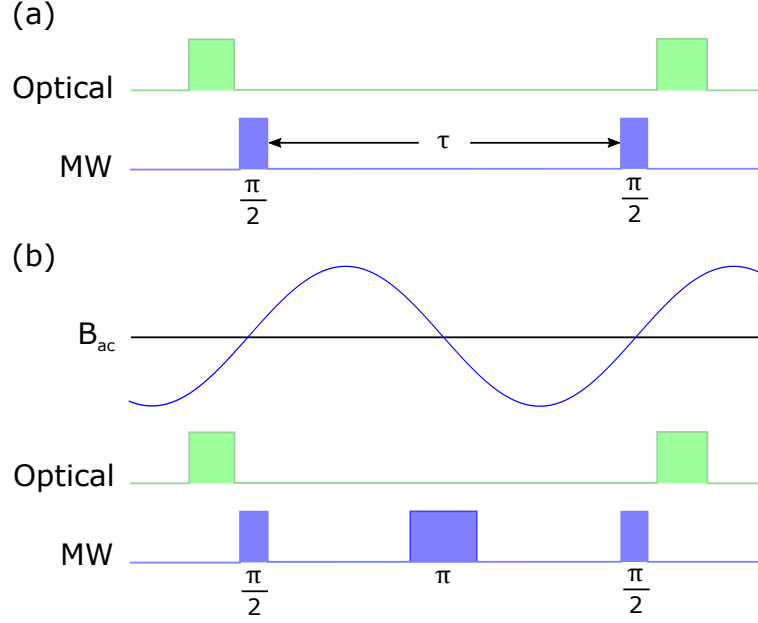$$\eta_{ramsey} \sim \frac{\hbar}{g_s\mu_B} \frac{1}{C\sqrt{N\beta T_2^*}}.$$

Figure 1-2: **Pulsed Magnetometry Sequences a)** Ramsey Sequence for DC magnetometry **b)** Hahn-Echo Sequence for AC magnetometry.

For AC magnetometry, the Ramsey sequence can be modified by bisecting the free precession interval τ with a single resonant π pulse. The pulse is precisely timed to occur at the node of the oscillating field [Fig 1-2(b)] and deems to swap the accumulated phase from the $|1\rangle$ to the $|0\rangle$ state. For slow components of the external magnetic noise, the swap allows the second half of the free precession interval to compensate for phase randomization acquired during the first half of the interval. Using this sequence, τ can be increased to the homogeneous spin coherence time T_2 often orders of magnitude longer than T_2^*. The sensitivity for sensing an AC field is then improved when compared to sensing a DC field by a factor $\sqrt{T_2^*/T_2}$. This sequence is known as a Hahn-Echo sequence but AC magnetometry can be performed by more complex dynamical decoupling techniques [6, 27].

1.3.4   Rabi oscillations

When an on- or near-resonant MW pulse is applied to a ground state transition in the NV, e.g. $|0\rangle \rightarrow |+1\rangle$, the NV spin state population will oscillate coherently between these two levels at a rate called the Rabi frequency (Ω_R). This rate of oscillation
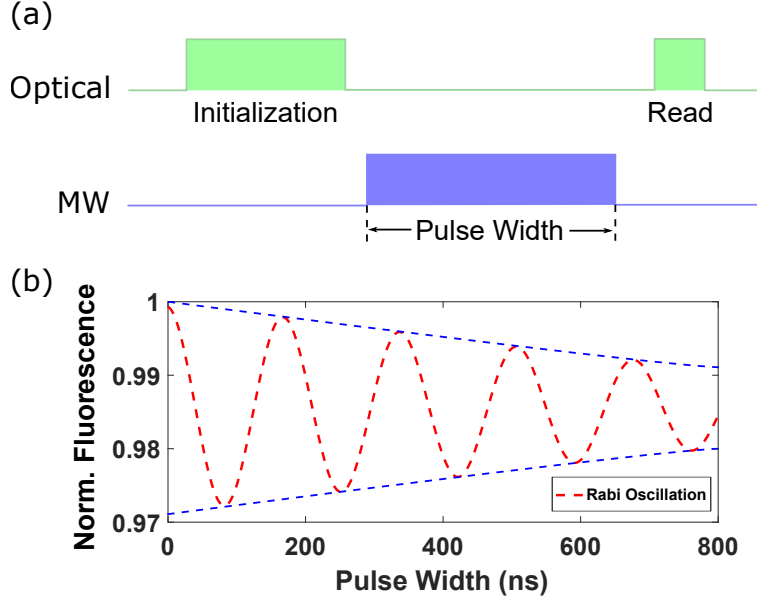
(a)

Optical — Initialization — Read

MW — Pulse Width

(b)

Figure 1-3: **Rabi pulse sequence and oscillations a)** Pulse sequence for detecting Rabi oscillation between two spin sublevels **b)** Example Rabi oscillations ($- -$) with exponential decay envelope ($- -$).

is a function of the amplitude of the applied MW pulse. It is commonly measured by consecutively applying a polarizing laser pulse, a MW pulse, and a readout pulse [Fig. 1-3 (a)] and varying the MW pulse length after each iteration.

Fig. 1-3 (b) plots a typical Rabi curve and its decay envelope. If the NV is originally in $|0\rangle$ (ie. at time $t = 0$) and we let the system evolve, then the probability that the spin is found in $|+1\rangle$ is $P_{+1} = \left(\frac{\omega_1}{\Omega_R}\right)^2 sin^2\left(\frac{\Omega_R t}{2}\right)$ where $\Omega_R = \sqrt{(\omega - \omega_0)^2 - \omega_1^2}$ is the Rabi frequency, ω is the radial frequency of the oscillating field $B_1(\omega)$, ω_0 the resonant frequency of the transition, and ω_1 the (max) Rabi frequency at zero detuning. At resonance, the driving frequency is $\omega = \omega_0$ and the transition probability becomes $P_{+1} = sin^2\left(\frac{\omega_1 t}{2}\right)$. In order to therefore drive the entire population from e. g. $|0\rangle$ to $|+1\rangle$ as needed in, for example, the Hahn-Echo sequence described in 1.3.3, one needs to apply a pulse length such that $sin^2\left(\frac{\omega_1 t}{2}\right) = 1$ which is satisfied when $t = \frac{pi}{\omega_1}$. For a Ramsey-type sequence that requires an equal superposition between $|0\rangle$ and $|+1\rangle$ one needs to apply half the π pulse, $t = \frac{\pi}{2\omega_1}$. The Rabi oscillations however decay due to inhomogeneous broadening of the ensembles linewidth, and are therefore fit by the decaying envelope $\exp\{-(PW/T)^p\}$, where PW is the pulse width and T and p are

19

fit parameters.

1.4 NV-MW coupling

calculate coupling between NV center and MW photons in cavity.

Chapter 2

The Loop Gap Resonator

As mentioned in the introduction, for many applied modalities within applications that use NV centers, the MW field (often denoted B_1 from NMR nomenclature), requires both high power and high uniformity to achieve high-fidelity quantum-state manipulation over the entire sample volume. As volumes are increased however, to maximize the number of NVs addressed without having a deleterious affect on the optimal measurement time, applying such a field becomes more difficult using standard approaches such as shorted coaxial loops [9, 8], microstrip waveguides [1, 20], and 50 Ω-terminated coaxial transmission lines [43, 28, 45, 44]. These broadband approaches allow arbitrary drive frequencies, however, the lack of resonant enhancement forces a compromise between the addressed volume and field strength. Section ?? describes how planar lumped-element resonators such as split-ring resonators [4], planar-ring resonators [45, 35], omega resonators [40, 21, 38], and patch antennas [45] can improve coupling between the resonator and the NVs by resonantly enhancing the local B_1 field and thus enable MW driving over larger regions, but at the expense of bandwidth and thus, for an operational magnetometer, dynamic range. Additionally, planar resonators are shown to yield poor homogeneity in the planes normal to their surface and therefore lend themselves less to bulk magnetometry than to 2D imaging applications. To address this shortcoming 3D resonators and cavities can be employed such as enclosed metallic cavity resonators [34], enclosed dielectric resonators [5, 25, 11], open dielectric resonators [23], and three-dimensional lumped element res-

onators [2], which provide good field homogeneity and strong resonantly enhanced fields, but offer little to no optical access. Since all-optical initialization and readout is a primary benefit for many solid-state spin systems, including NV diamond [13], such a trade-off is incompatible with many existing and envisioned applications [36].

To address this current shortcoming a three-dimensional tunable loop-gap resonator (LGR), based on the anode block of a cavity magnetron, is used to achieve desired MW drive strengths homogeneously over large areas. Additionally, its open geometry allows for good optical accessibility for interrogation volumes centered within the LGR cavity. Traditionally, the LGR has been used either as the anode block of cavity magnetrons [], or as a low frequency (2-4 GHz) lumped element resonator for electron paramagnetic resonance (EPR) studies [].

2.1   Resonant Enhancement of the MW field

The LGR acts classically like an underdamped oscillator. It stores MWs within the confines of its geometrical structure by allowing the energy to oscillate back and forth between an electric and magnetic potential. At resonance (ω_0) the ratio of magnetic energy to electric energy is 1. The time $\tau_r ing$ the energy can oscillate before its power is reduced by a factor of $1/e$ is characterized by a dimensionless quantity called the Q-factor. It's defined by the following ratio

$$Q = \omega_0 \frac{StoredEnergy}{PowerLoss}.$$ (2.1)

If the resonator is therefore continuously fed by an external power source an enhancement of the stored energy takes place that is proportional to both the current supplied and the Q-factor of the cavity. The magnitude of the magnetic flux within the center cavity (for a cylindrical resonator) is then given by

$$|B_1| \approx \frac{\mu_0}{2r} \cdot I \cdot \sqrt{Q},$$ (2.2)

22

where μ_0 is the vacuum permeability, I is the supplied current, and r is the cylinder radius. It's therefore clear that a resonant enhancement of the magnetic field amplitude is induced which is proportional to the square root of the Q-factor.

2.2 Model

whatever

2.2.1 Lumped element solutions

Theoretical framework for analyzing LGR for m loops and n gaps including field distribution calculations

2.2.2 Field based solutions

Theory giving solutions of LGR using bessel functions

2.2.3 Coupling

Theory of coupling (mutual inductance, capcitance, etc)

2.3 LGR Design

Due to the loop gap resonator's existence since the early 20th century [10] it has seen many variations and modifications all designed with particular applications in mind. Figure 2-1 shows the cross section of a variety of LGRs including rising-sun, vane, slot, and hole-and-slot type resonators. EPR experiments at low frequencies (2-4 GHz) quickly adopted the LGR as opposed to more traditional TE_{102} type cavities because of the LGRs smaller size relative to the frequency of excitation. At 3 GHz the side length of the TE_{102} cavity must be at least 5 cm which reduces drastically the cavity filling factor–a parameter necessary for the sensitivity of an EPR signal. Since many aspects of EPR spectroscopy are mirrored in NV magnetometry (requirement of

homogeneous and strong microwave signals, frequency of operation, etc.) we selected to design a hole-and-slot type resonator found in many EPR applications [].
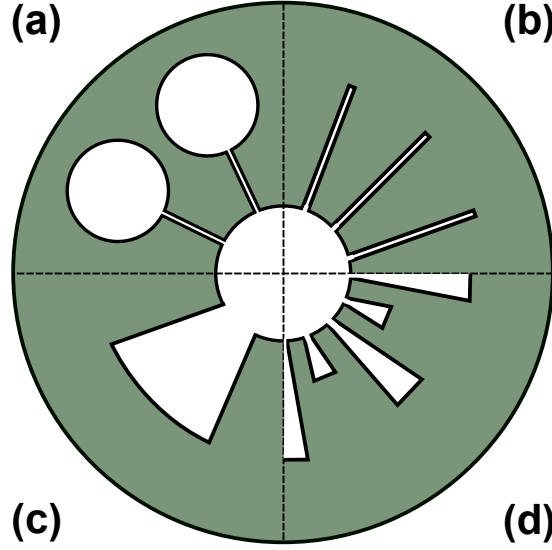

Figure 2-1: **Loop Gap Resonator Variations a)** Hole and Slot. **b)** Slot. **c)** Vane. **d)** Rising Sun - type

2.3.1 LGR

A standard hole-and-slot LGR with n outer loops can be approximated as n coupled LC resonators oscillating in tandem at a target resonant frequency [42]. Circulating currents around the central and outer loops create a total inductance, as found in section 2.2.1,

$$L \approx \frac{L_c n L_o}{n L_o + L_c},$$ (2.3)

and charge at the gap walls create a total capacitance C, which is given by

$$C \approx \frac{\epsilon_r \epsilon_o A}{nd},$$ (2.4)

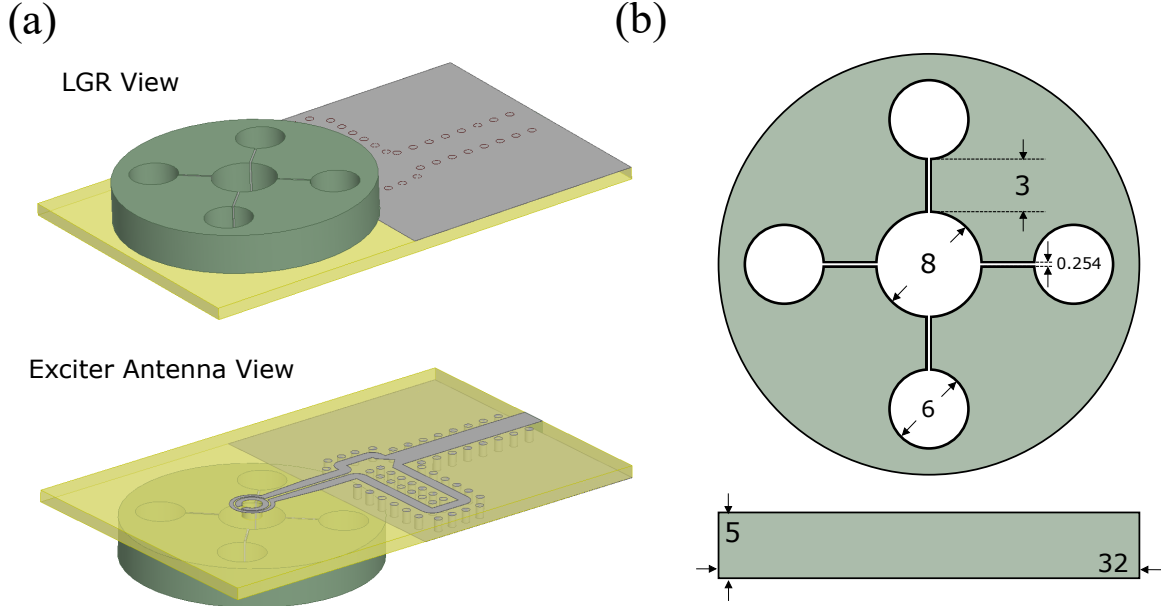which, when combined yield the resonant frequency

Figure 2-2: **Rendering and Wire Diagram of Loop Gap Resonator a)** The metallic resonator employs a five-loop four-gap architecture. Microwaves are coupled into the LGR via the exciter antenna, which is fabricated on a printed circuit board. **b)** Line drawing of the LGR. All dimensions are in mm. Optional mounting holes and radial access port for laser excitation are now shown.

$$f_0 = \frac{1}{2\pi\sqrt{LC}}. \tag{2.5}$$

In practice, the central loop diameter is set to $\sim 5 - 10$ mm, corresponding to the typical size of a diamond plate. The outer loop diameters are chosen to match the inner diameters within a small factor to ensure return flux is captured and does not extend into the annular region around the LGR []. Since the outer and inner loops set the effective inductance of the resonator, the gap area A is constrained by the dual LGR design objectives of (i) maintaining optical accessibility, which limits the thickness of the device, and (ii) bounding f_0 above the target resonant frequency in order to allow for further tuning vie dielectric shims (discussed in section 2.4). Additionally, while increasing the number n of loops and gaps can improve B_1 uniformity [32] and lower the LGR's resonant frequency, this approach results in a denser mode spectrum [17] and increases the likelihood of cross-mode excitations deleteriously altering the field distribution within the central loop. As a compromise,

the design employs $n = 4$ outer loops [Fig. 2-2 (a)] allowing for sufficient uniformity while locating the closest eigenmode more than 1.5 GHz below the TE_{10} eigenmode [Fig ??].

The LGR in this work therefore consists of a central loop with radius $r_c = 4$ mm surrounded by four symmetrically arranged outer loops of radius $r_o = 3$ mm as shown in Figure 2-2 (b). The outer loops return magnetic flux to the central loop and therefore oscillate antisymmetrically with the central loop (π out of phase). The side walls of the capacitive gaps are separated by $d = 254$ μm. With these dimensions, using equations 2.3.1 and 2.3.1, $L = 8.7$ nH and $C = 0.17$ pF, resulting in an expected resonant frequency for the naked air-gapped LGR of $f_0 = 4.1$ GHz, approximately 1.2 GHz above the NV resonance frequencies.

An eigenfrequency simulation of the resonator using the geometrical parameters listed above was completed in ANSYS HFSS and the distribution of the magnetic flux density (B_1) for the TE_{10} mode is depicted in Figure 2-5. As mentioned above, for this mode the center loop oscillates π radians out of phase with the outer loops. For the air-gapped resonator, HFSS returns a real eigenfrequency at 4.57 GHz (depicted in Figure 2-5)

2.4   Tuning

Talk about tuning the LGR using sapphire shims; why use sapphirie shims? etc etc etc

2.5   Excitation Design

To couple MW power into the LGR we utilized two separate methods, each to be used for different NV applications. For magnetic microscopy, complete 2π steradian optical access to the center cavity is of the utmost importance. For such modalities lateral coupling using a shorted coaxial loop [Figure ?? (a)] can be used to minimize the blocking of optical access to the central loop. Using this method, resonator coupling
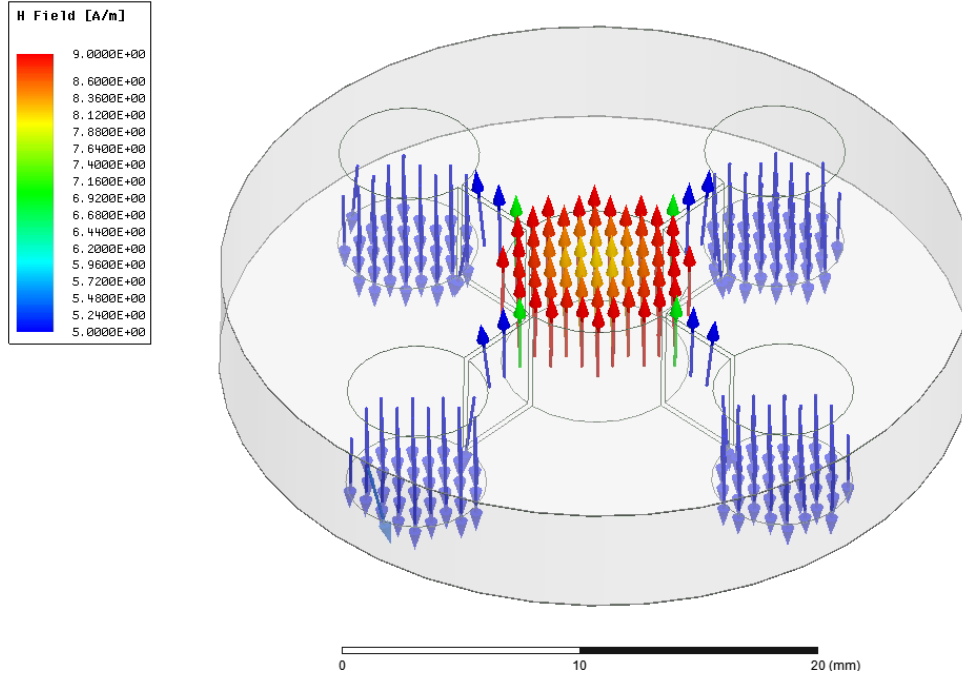
Figure 2-3: **Eigenfrequency solution to LGR** Eigenfrequency solution for TE_{10} mode. The outer loops are oscillating *pi* radians out of phase with center loop

(described in section 2.2.3) is modified by changing the coaxial loop position in z relative to the LGR. In this way the LGR can be quickly and effectively critically coupled for any shim configuration (ie. resonant frequency) [Figure **??** (b)].

Discussion with images of coupling using shorted coax loop.

More robust coupling for implementable device

Discussion of split ring exciter antenna and design outline of feedline and balun and design process of stepping through circuit etc.

center loop coupling with split ring resonator. Sonnet program design or split loop (snap shots from program and S11 etc)

2.6   Matching

As mentioned above, for lateral coupling using a coaxial loop the LGR can be quickly matched to the feedline by varying the distance z between the loop and the resonator.

Talk about matching using coupling parameter and etc. (quick overview of matching using mathematical framework).
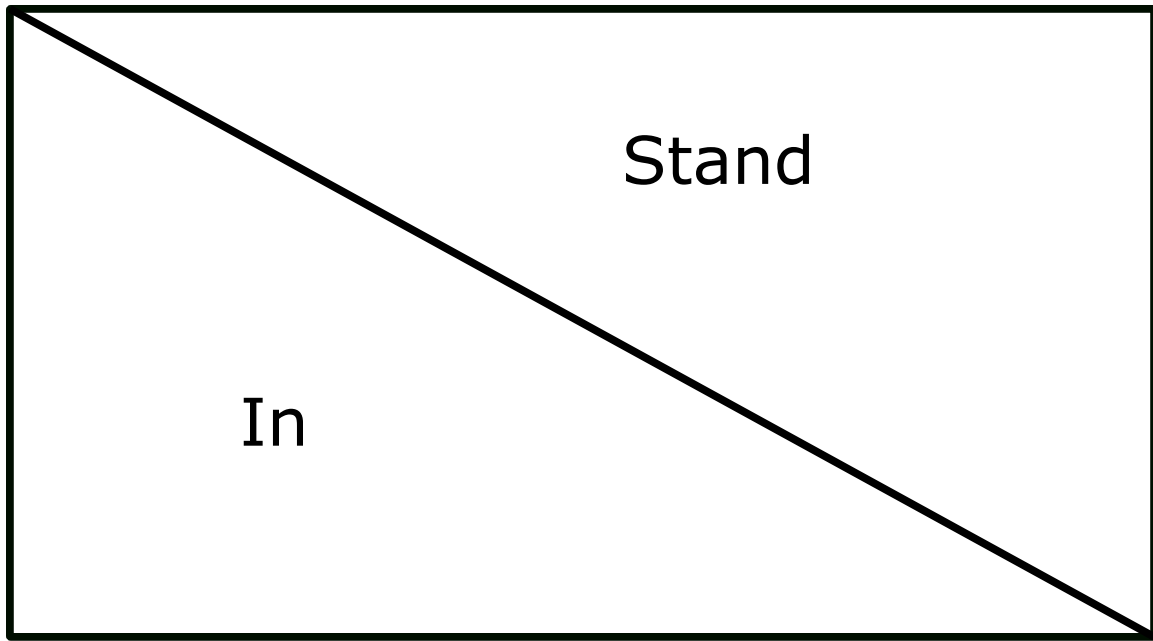
Figure 2-4: **Eigenfrequency solution to LGR a)** STANDIN. PLEASE REPLACE

Talk about matching using Lateral loop coupling

Talk about Balun design (w/ sonnet)

Talk about board design (w/ sonnet)
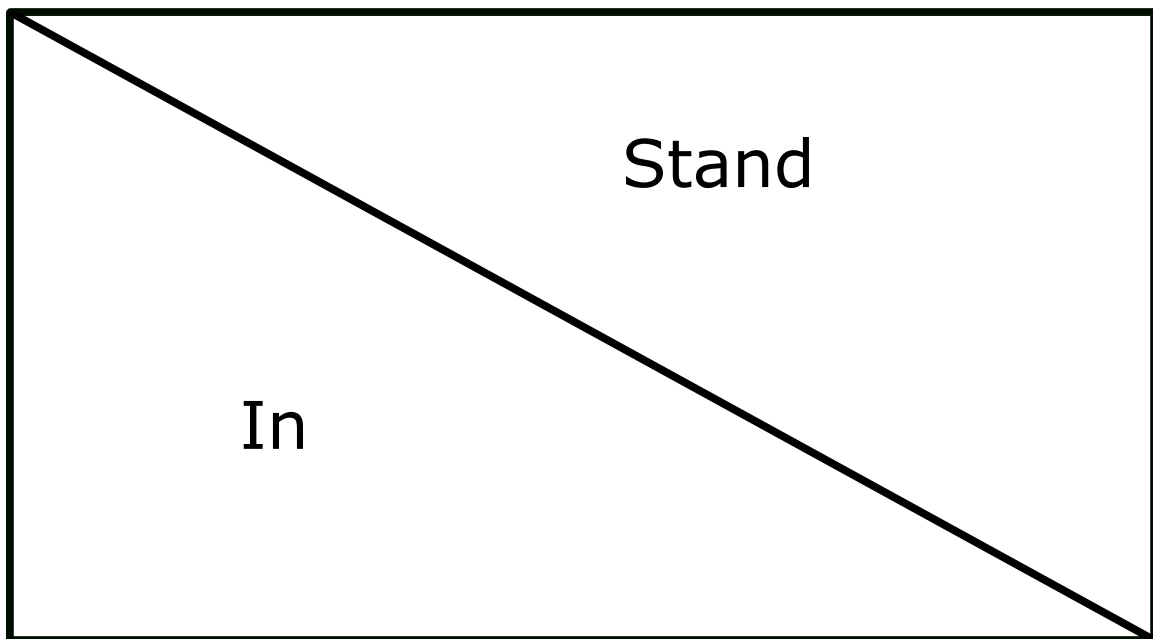
Talk about additional matching using stub tuner.

Figure 2-5: **Eigenfrequency solution to LGR a)** STANDIN. PLEASE REPLACE

Chapter 3

LGR Performance and Field Characterization

Whatever

3.1 Quality Factor

Qualtiy factor importance etc. Low Q importance for CW application (ie. fitting all resonances in for wide dynamic range magnetometer) and for pulsed (minimize ring down ie dead time between subsequent pulses)

Discussion on using concatinated pulses to mitigate long ring down as a method to use high Q resonators (like copper resonator) even though their ring down time is long. Attempt to work out the math on these pulses or give a small mathematical description of dead time mitigating pulses. Ie active cancellation

3.1.1 Calculation

calculating Q in different coupled regimes

3.1.2 Measurement

Measuring the Q using ring-down method and bandwidth method

3.1.3 Ringdown time

short mathematical walkthrough of calculating ring down time from Q factor. From Jackson preferably.

3.2 Measuring Magnetic Field

3.2.1 Experimental setup

talk about confocal microscope, give outline schematic of setup

3.2.2 Measurement

Talk about experiment taking Rabi data, ie. Rabi pulse sequence, moving resonator, checking ESR, choosing ESR etc.

3.2.3 B_1 from Rabi

calculating B_1 from Rabi frequency using rotating wave approx. etc, essentially where sqrt(3) comes from.

Appendix A

Tables

Table A.1: Armadillos

Armadillos	are
our	friends

Appendix B

Figures

Figure B-1: Armadillo slaying lawyer.

Figure B-2: Armadillo eradicating national debt.

Bibliography

[1] Paolo Andrich, F Charles, Xiaoying Liu, Hope L Bretscher, Jonson R Berman, F Joseph Heremans, Paul F Nealey, and David D Awschalom. Long-range spin wave mediated control of defect qubits in nanodiamonds. *npj Quantum Information*, 3(1):28, 2017.

[2] A. Angerer, T. Astner, D. Wirtitsch, H. Sumiya, S. Onoda, J. Isoya, S. Putz, and J. Majer. Collective strong coupling with homogeneous Rabi frequencies using a 3D lumped element microwave resonator. *Applied Physics Letters*, 109(3):033508, July 2016.

[3] Gopalakrishnan Balasubramanian, IY Chan, Roman Kolesov, Mohannad Al-Hmoud, Julia Tisler, Chang Shin, Changdong Kim, Aleksander Wojcik, Philip R Hemmer, Anke Krueger, et al. Nanoscale imaging magnetometry with diamond spins under ambient conditions. *Nature*, 455(7213):648, 2008.

[4] K. Bayat, J. Choy, M. Farrokh Baroughi, S. Meesala, and M. Loncar. Efficient, Uniform, and Large Area Microwave Magnetic Coupling to NV Centers in Diamond Using Double Split-Ring Resonators. *Nano Letters*, 14:1208–1213, March 2014.

[5] J. D. Breeze, J. Sathian, E. Salvadori, N. McN. Alford, and C. W. M. Kay. Continuous-wave room-temperature diamond maser. *ArXiv e-prints*, October 2017.

[6] H. Y. Carr and E. M. Purcell. Effects of Diffusion on Free Precession in Nuclear Magnetic Resonance Experiments. *Physical Review*, 94:630–638, May 1954.

[7] Lilian Childress and Ronald Hanson. Diamond nv centers for quantum computing and quantum networks. *MRS bulletin*, 38(2):134–138, 2013.

[8] M. Chipaux, A. Tallaire, J. Achard, S. Pezzagna, J. Meijer, V. Jacques, J.-F. Roch, and T. Debuisschert. Magnetic imaging with an ensemble of nitrogen vacancy-centers in diamond. *European Physical Journal D*, 69:166, July 2015.

[9] H. Clevenson, M. E. Trusheim, C. Teale, T. Schröder, D. Braje, and D. Englund. Broadband magnetometry and temperature sensing with a light-trapping diamond waveguide. *Nature Physics*, 11:393–397, May 2015.

[10] George Briggs Collins. *Microwave magnetrons*, volume 6. McGraw-Hill Book Company, 1948.

[11] D. L. Creedon, J.-M. Le Floch, M. Goryachev, W. G. Farr, S. Castelletto, and M. E. Tobar. Strong coupling between P 1 diamond impurity centers and a three-dimensional lumped photonic microwave cavity. *Physical Review B*, 91(14):140408, April 2015.

[12] C. L. Degen. Scanning magnetic field microscope with a diamond single-spin sensor. *Applied Physics Letters*, 92(24):243111, June 2008.

[13] M. W. Doherty, N. B. Manson, P. Delaney, F. Jelezko, J. Wrachtrup, and L. C. L. Hollenberg. The nitrogen-vacancy colour centre in diamond. *Physics Reports*, 528:1–45, July 2013.

[14] F. Dolde, H. Fedder, M. W. Doherty, T. Nöbauer, F. Rempp, G. Balasubramanian, T. Wolf, F. Reinhard, L. C. L. Hollenberg, F. Jelezko, and J. Wrachtrup. Electric-field sensing using single diamond spins. *Nature Physics*, 7:459–463, June 2011.

[15] A Dréau, M Lesik, L Rondin, P Spinicelli, O Arcizet, J-F Roch, and V Jacques. Avoiding power broadening in optically detected magnetic resonance of single nv defects for enhanced dc magnetic field sensitivity. *Physical Review B*, 84(19):195204, 2011.

[16] M. V. G. Dutt, L. Childress, L. Jiang, E. Togan, J. Maze, F. Jelezko, A. S. Zibrov, P. R. Hemmer, and M. D. Lukin. Quantum Register Based on Individual Electronic and Nuclear Spin Qubits in Diamond. *Science*, 316, June 2007.

[17] W. Froncisz and J. S. Hyde. The loop-gap resonator: a new microwave lumped circuit ESR sample structure. *Journal of Magnetic Resonance*, 47:515–521, 1982.

[18] T. Gaebel, M. Domhan, I. Popa, C. Wittmann, P. Neumann, F. Jelezko, J. R. Rabeau, N. Stavrias, A. D. Greentree, S. Prawer, J. Meijer, J. Twamley, P. R. Hemmer, and J. Wrachtrup. Room-temperature coherent coupling of single spins in diamond. *Nature Physics*, 2:408–413, June 2006.

[19] J. S. Hodges, N. Y. Yao, D. Maclaurin, C. Rastogi, M. D. Lukin, and D. Englund. Timekeeping with electron spin states in diamond. *Physical Review A*, 87(3):032118, March 2013.

[20] V. R. Horowitz, B. J. Alemán, D. J. Christle, A. N. Cleland, and D. D. Awschalom. Electron spin resonance of nitrogen-vacancy centers in optically trapped nanodiamonds. *Proceedings of the National Academy of Science*, 109:13493–13497, August 2012.

[21] A. Horsley, P. Appel, J. Wolters, J. Achard, A. Tallaire, P. Maletinsky, and P. Treutlein. Microwave device characterisation using a widefield diamond microscope. *ArXiv e-prints*, February 2018.

[22] Kasper Jensen, Pauli Kehayias, and Dmitry Budker. Magnetometry with Nitrogen-Vacancy Centers in Diamond. In *High Sensitivity Magnetometers*, pages 553–576. Springer, 2017.

[23] P. Kapitanova, V. Soshenko, V. Vorobyov, D. Dobrykh, S. Bolshedvorskiih, V. Sorokin, and A. Akimov. Dielectric resonator antenna for coupling to NV centers in diamond. In *American Institute of Physics Conference Series*, volume 1874 of *American Institute of Physics Conference Series*, page 030017, September 2017.

[24] S. Kitazawa, Y. Matsuzaki, S. Saijo, K. Kakuyanagi, S. Saito, and J. Ishi-Hayase. Vector-magnetic-field sensing via multifrequency control of nitrogen-vacancy centers in diamond. *Physical Review A*, 96(4):042115, October 2017.

[25] J.-M. Le Floch, N. Delhote, M. Aubourg, V. Madrangeas, D. Cros, S. Castelletto, and M. E. Tobar. Towards achieving strong coupling in three-dimensional-cavity with solid state spin resonance. *Journal of Applied Physics*, 119(15):153901, April 2016.

[26] J. R. Maze, A. Gali, E. Togan, Y. Chu, A. Trifonov, E. Kaxiras, and M. D. Lukin. Properties of nitrogen-vacancy centers in diamond: the group theoretic approach. *New Journal of Physics*, 13(2):025025, February 2011.

[27] S. Meiboom and D. Gill. Modified Spin-Echo Method for Measuring Nuclear Relaxation Times. *Review of Scientific Instruments*, 29:688–691, August 1958.

[28] M. Mrózek, J. Mlynarczyk, D. S. Rudnicki, and W. Gawlik. Circularly polarized microwaves for magnetic resonance study in the GHz range: Application to nitrogen-vacancy in diamonds. *Applied Physics Letters*, 107(1):013505, July 2015.

[29] P. Neumann, I. Jakobi, F. Dolde, C. Burk, R. Reuter, G. Waldherr, J. Honert, T. Wolf, A. Brunner, J. H. Shim, D. Suter, H. Sumiya, J. Isoya, and J. Wrachtrup. High-Precision Nanoscale Temperature Sensing Using Single Defects in Diamond. *Nano Letters*, 13:2738–2742, June 2013.

[30] L. M. Pham. *Magnetic field sensing with nitrogen-vacancy color centers in diamond*. PhD thesis, Harvard University, 2013.

[31] Linh My Pham, David Le Sage, Paul L Stanwix, Tsun Kwan Yeung, D Glenn, Alexei Trifonov, Paola Cappellaro, PR Hemmer, Mikhail D Lukin, Hongkun Park, et al. Magnetic field imaging with nitrogen-vacancy ensembles. *New Journal of Physics*, 13(4):045021, 2011.

[32] W. Piasecki and W. Froncisz. Field distributions in loop-gap resonators. *Measurement Science and Technology*, 4:1363–1369, December 1993.

[33] L. Rondin, J.-P. Tetienne, T. Hingant, J.-F. Roch, P. Maletinsky, and V. Jacques. Magnetometry with nitrogen-vacancy defects in diamond. *Reports on Progress in Physics*, 77(5):056503, May 2014.

[34] B. C. Rose, A. M. Tyryshkin, H. Riemann, N. V. Abrosimov, P. Becker, H.-J. Pohl, M. L. W. Thewalt, K. M. Itoh, and S. A. Lyon. Coherent Rabi Dynamics of a Superradiant Spin Ensemble in a Microwave Cavity. *Physical Review X*, 7(3):031002, July 2017.

[35] Kento Sasaki, Yasuaki Monnai, Soya Saijo, Ryushiro Fujita, Hideyuki Watanabe, Junko Ishi-Hayase, Kohei M Itoh, and Eisuke Abe. Broadband, large-area microwave antenna for optically detected magnetic resonance of nitrogen-vacancy centers in diamond. *Review of Scientific Instruments*, 87(5):053904, 2016.

[36] R. Schirhagl, K. Chang, M. Loretz, and C. L. Degen. Nitrogen-Vacancy Centers in Diamond: Nanoscale Sensors for Physics and Biology. *Annual Review of Physical Chemistry*, 65:83–105, April 2014.

[37] J. M. Schloss, J. F. Barry, M. J. Turner, and R. L. Walsworth. Simultaneous Broadband Vector Magnetometry Using Solid-State Spins. *ArXiv e-prints*, March 2018.

[38] David A. Simpson, Robert G. Ryan, Liam T. Hall, Evgeniy Panchenko, Simon C. Drew, Steven Petrou, Paul S. Donnelly, Paul Mulvaney, and Lloyd C. L. Hollenberg. Electron paramagnetic resonance microscopy using spins in diamond under ambient conditions. *Nature Communications*, 8(1):458, 2017.

[39] J. M. Taylor, P. Cappellaro, L. Childress, L. Jiang, D. Budker, P. R. Hemmer, A. Yacoby, R. Walsworth, and M. D. Lukin. High-sensitivity diamond magnetometer with nanoscale resolution. *Nature Physics*, 4:810–816, October 2008.

[40] Y. Twig, E. Dikarov, and A. Blank. Ultra miniature resonators for electron spin resonance: Sensitivity analysis, design and construction methods, and potential applications. *Molecular Physics*, 111:2674–2682, October 2013.

[41] T. Wolf, P. Neumann, K. Nakamura, H. Sumiya, T. Ohshima, J. Isoya, and J. Wrachtrup. Subpicotesla Diamond Magnetometry. *Physical Review X*, 5(4):041001, October 2015.

[42] R. L. Wood, W. Froncisz, and J. S. Hyde. The loop-gap resonator. II. Controlled return flux three-loop, two-gap microwave resonators for ENDOR and ESR spectroscopy. *Journal of Magnetic Resonance*, 58:243–253, 1984.

[43] L.-L. Yang, Q.-Q. Liu, X.-Y. Pan, and D.-M. Chen. Design and Application of a Near Field Microwave Antenna for the Spin Control of Nitrogen-Vacancy Centers. *Chinese Physics Letters*, 27(3):038401, March 2010.

[44] Chen Zhang, Heng Yuan, Ning Zhang, Lixia Xu, Jixing Zhang, Bo Li, and Jiancheng Fang. Vector magnetometer based on synchronous manipulation of nitrogen-vacancy centers in all crystal directions. *Journal of Physics D: Applied Physics*, 51(15):155102, 2018.

[45] Ning Zhang, Chen Zhang, Lixia Xu, Ming Ding, Wei Quan, Zheng Tang, and Heng Yuan. Microwave magnetic field coupling with nitrogen-vacancy center ensembles in diamond with high homogeneity. *Applied Magnetic Resonance*, 47(6):589–599, 2016.